Universität Hamburg
DER FORSCHUNG | DER LEHRE | DER BILDUNG

FAKULTÄT
FÜR MATHEMATIK, INFORMATIK
UND NATURWISSENSCHAFTEN

LEIBNIZ-INSTITUTE
OF
ATMOSPHERIC
PHYSICS
IAP

Bachelor Thesis

# Investigation of Noctilucent Clouds using High Resolution Lidar Measurements

**Jon Petersen**

jon.petersen@studium.uni-hamburg.de
Course: B. Sc. Meteorology
Matr.-No.: 6939930
Semester: 06

Primary supervisor: Prof. Dr. Stefan Bühler (UHH)
Secondary supervisor: Dr. Michael Gerding (IAP)

Submission: December 16, 2019

# Investigation of Noctilucent Clouds using High Resolution Lidar Measurements

# Abstract

Noctilucent clouds (NLC) are mesospheric ice clouds that occur at high latitudes in the summer hemisphere. These clouds can be used as tracers for gravity wave (GW) activities, as NLCs are modulated by them. The investigation of gravity waves is of particular importance for the understanding of atmospheric circulation as they transport momentum and energy through the entire atmosphere. In Kühlungsborn (54° N, 12° E), a daylight lidar was launched in 2010, which allows to observe wave phenomena with a resolution of 33 s in time and 15 m in space. In this thesis, three case studies of strong events were examined. For earlier investigations in Kühlungsborn, a resolution of 33 s in time and 195 m in height with a smoothing of typically $\pm 7$ min and $\pm 1$ height bin was used. It turns out, however, that many structures in the NLCs occur on smaller scales, since the layer thickness in the clouds is 44 % lower than the previous vertical resolution. On June 21, 2019, several layers with an average distance of 265 m above each other appeared. Local instabilities are assumed to be the cause, since GW have a significantly larger vertical wavelength. A spectral analysis of the vertical displacement of the cloud shows signatures of large scale gravity waves, as well as turbulence in higher frequency ranges. The average slope of the spectrum is -2.6, similar to the Nastrom-Gage spectrum for large scale gravity waves with a slope of -3.

# Zusammenfassung

Nachtleutende Wolken (NLC) sind mesosphererische Eiswolken, welche in der Sommerhemisphäre in hohen Breiten auftreten. Diese Wolken können als Tracer für Schwerewellen (GW) Aktivitäten genutzt werden, da NLCs von diesen modulliert werden. Die Untersuchung von Schwerewellen sind für das Verständnis von atmsphärischen Zirkluation von besonderer Bedeutung, da sie Impuls und Energie durch die ganze Atmosphere transportieren. In Kühlungsborn (54° N, 12° O) wurde 2010 ein tageslichtfähiges Lidar in Betrieb genommen, was es ermöglicht, Wellenphänomene mit einer zeitlichen Auflösung von 33 s und einer räumlichen Auflösung von 15 m zu beobachten. In dieser Arbeit wurden drei Fallbeispiele von starken Ereignissen untersucht. Für frühere Untersuchungen wurde in Kühlungsborn eine zeitliche Auflösung von 33 s und eine räumliche Auflösung von 195 m mit einer Glättung von typischerweise $\pm 7$ min und $\pm 1$ Höhenintervall verwendet. Es stellt sich jedoch heraus, dass viele Strukturen in den NLCs auf kleineren Skalen liegen, da die Schichtdicke in den Wolken 44 % geringer als die bisherige vertikale Auflösung ist. Am 21. Juni 2019 sind mehrere Schichten mit einem durchschnittlichen Abstand von 265 m übereinander aufgetreten. Als Ursache werden lokale Instabilitäten vermutet, da GW eine deutlich größere vertikale Wellenlänge besitzen. Eine Spektralanalyse der vertikalen Auslenkung der Wolke zeigt Signaturen von großskaligen Schwerewellen, sowie Turbulenz in größeren Frequenzbereichen. Die durschnittliche Steigung des Spektrums beträgt -2.6, was dem Nastrom-Gage Spektrum für großskalige Schwerewellen mit einer Steigung von -3 ähnelt.

# Contents

# List of Figures

# 1 Introduction

## 1.1 Motivation

The aim of this bachelor thesis is to determine whether high resolution lidar measurements of noctilucent clouds (NLC) made by the Leibniz-Institute of Atmospheric Physics (IAP) in Kühlungsborn (54° N, 12° E), Germany, could be used to study gravity waves. Gravity waves play a major role in atmospheric dynamics, because the propagation and eventual breaking transports and deposits momentum and energy on a horizontal and especially vertical scale (Holton and Alexander, 2000; Fritts and Alexander, 2003). Typically, models only use linear parametrization schemes to describe this long distance energy transport, which results in an higher variance between simulations and observation (e.g., Kim et al., 2003). Therefore, additional measurements and observational data are necessary for validation and further improvements of those parametrizations (Geller et al., 2013). Until today, lidar measurements of noctilucent clouds from Kühlungsborn where used with a resolution of 33 s in time and 195 m in height, but smoothed over $\pm 7$ min and $\pm 1$ height bin to study the NLCs, e.g. the diurnal variations of midlatitude NLC parameters (Gerding et al., 2013). The resolution for the investigations in this thesis is 33 seconds integration time and a vertical resolution of 15 m.
The structure of this thesis is described in the following paragraph. First of all, the underlying principles for the thesis will be explained in Section 1.2-1.4, followed by a description of the data set which was used (Section 2.1) and a detailed description of the lidar in Section 2.2. The preprocessing and methods used are shown in Section 2.3. Chapter 3 reviews and discusses different cloud properties, a multi layer analysis and the spectral analysis of the vertical variable backscatter coefficient that were done. Finally, Chapter 4 concludes the results, summarizes the findings of this thesis and gives an outlook on possible further investigations.

## 1.2 Noctilucent Clouds

First observations of noctilucent clouds go back to the year 1885 and first height measurements were published by Jesse ten years later (Jesse, 1896; Craig, 2016). Since then, this phenomenon has been observed and analyzed repeatedly (Vestine, 1934; Størmer, 1935; Ludlam, 1957; Craig, 2016). Nowadays, observations of NLC include the use of numerous measurements techniques, e.g. satellite, optical and airborne. For this thesis, lidar

measurements are used to get a time series of the altitude distribution at a single location. Typically, NLC only occur in summer in the upper mesosphere and are only visible by eye when the sun is 6 to 12 degrees below the horizon. Clouds usually do not occur at such high altitudes, due to the very low water vapor concentrations and low pressure. For clouds to form under such circumstances, very low temperatures are required which can not be understood on radiative grounds alone. Those temperatures are only reached in late summer at high latitudes (polewards of $\sim 50^\circ$ latitude). Radiative calculations intuitively predict that the minimum temperatures occur over the winter pole, with temperatures gradually increasing toward the summer pole. In reality, however, the exact opposite is the case, due to the breaking of gravity waves, which is further discussed in Section 1.3. This effect results in the temperature profile shown in Figure 1.1. The profile is based on measurements from the lidar side in Kühlungsborn and was calculated by Gerding et al., 2008.

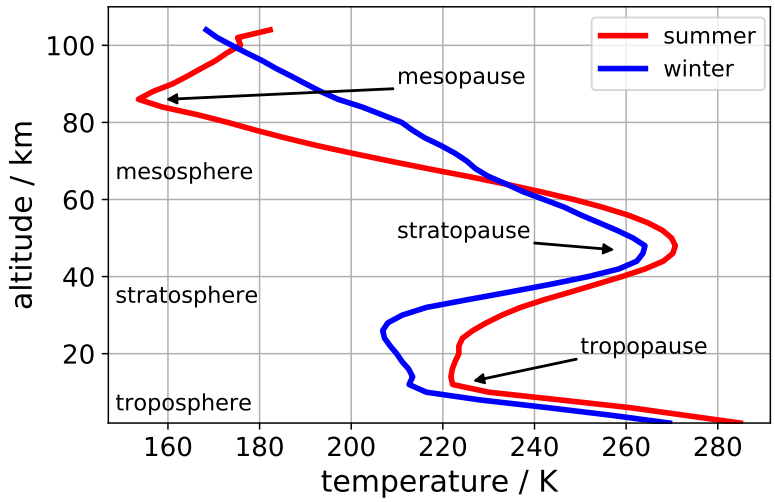


Figure 1.1: Temperature profiles from Kühlungsborn (54° N, 12° E), Germany, derived from lidar measurements and averaged over the summer months (JJA, red line) and winter months (DJF, blue line). The data is taken from Gerding et al., 2008. In addition, the layers of the atmosphere, as well as their boundaries are shown. Note that the winter mesopause is well above 100 km and therefore not shown.

## 1.3 Gravity Waves

In fluid dynamics, gravity waves (GW) are generated in a fluid at the interface between two media when the forces of gravity and buoyancy try to restore equilibrium. Atmospheric gravity waves are called internal waves, because they are within one fluid body. A gravity wave results when fluid is displaced from a position of equilibrium. The restoration of the fluid to equilibrium will produce a movement of the fluid back and forth. This oscillation around its equilibrium position can be associated with the Brunt-

Väisälä frequency given by

$$N^2 = \frac{g}{T}\left(\frac{dT}{dz} - \Gamma\right), \tag{1.1}$$

where $\Gamma$ ( -10 K/km) is the adiabatic lapse rate and $\frac{dT}{dz}$ is the temperature gradient of the ambient air. If $\Gamma < \frac{dT}{dz}$, the conditions are statically stable and the parcel can oscillate freely.
The dispersion relation for GW is given by

$$\omega_I^2 = \frac{N^2(k^2 + l^2) + f^2(m^2 + \frac{1}{4H^2})}{k^2 + l^2 + m^2 + \frac{1}{4H^2}} \tag{1.2}$$

with $f$ the Coriolis parameter, $H$ being the scale height and $k$, $l$ and $m$ being the zonal, meridional and vertical wavenumbers, respectively. An exact derivation can be found in Holton, 1973. Rewriting Equation 1.2 for the vertical wavenumber $m$ shows that GW can only exist with intrinsic frequencies between $|f|$ and $N$.

$$m^2 = \frac{(k^2 + l^2)(N^2 - \omega_I^2)}{\omega_I^2 - f^2} - \frac{1}{4H^2} \tag{1.3}$$

Furthermore, inertia-gravity waves are influenced by the Coriolis effect due to the Earth's rotation and are the common features in the atmospheric flows. Hines (1960) was the first to note the presence of small scale internal gravity waves at mesospheric heights, which originate from the troposphere to lower stratosphere and are mostly generated by the flow above orographic structures, convective instabilities, wind shears, jet streams, or wave–wave interactions (e.g., Fritts and Alexander, 2003). They propagate upward and eventually break due to nonlinear effects. Theses waves deposit their angular momentum (often called "wave drag"). This deposit triggers a meridional circulation from the summer to the winter pole. That implies upwelling over the summer pole and downwelling over the winter pole which cause adiabatic cooling and warming, respectively (Shepherd, 2000 and references therein). This leads to the non-intuitive temperature profile described in section 1.2. Apart from occasionally strong lower-atmospheric effects, the major wave influences occur in the middle atmosphere, between roughly 10 and 110 km altitudes because of decreasing density and therefore increasing wave amplitudes with altitude. Intrinsic periods of those inertia-gravity waves are close to $2\pi/f$, where $f$ is the Coriolis parameter. Vertical wavelengths range from 5 up to 20 km in the upper stratosphere and mesosphere (Fritts et al., 1988; Riggin et al., 1995; Li et al., 2007). Until now only simple parametrizations for the GW drag and the deposit of angular momentum have been used, often leading to big differences between the used models and the few available measurements (e.g., Kim et al., 2003). Therefore, more data is needed for validation and further improvements of those models (Geller et al., 2013).

## 1.4 Lidar and Scattering

Lidar is an acronym which stands for "**li**ght **d**etection **a**nd **r**anging" and is, along with radiowave detection and ranging (radar), one of the remote-sensing techniques that is the backbone of atmospheric profiling. Every lidar consists of a transmitter and a receiver unit. Short laser pulses are sent out into the atmosphere, where the light is scattered by molecules and aerosols (the different properties will be discussed later in this section). The receiving telescope collects the backscattered photons in the right wavelength domain as a function of time, which provides information about the strength of the scattering signal and the height, respectively. Optical analysis of the backscattered light is usually done before the detection and plays an important role for Raman lidar. For this thesis simply, an interference filter is placed in front of the detector. The filter suppresses light outside the transmission band, e.g., sunlight and therefore only light in a certain passband around the wavelength of interest is transmitted. The number of photon counts per time interval, e.g., 10 ns after emission of the laser pulse is stored. The resolved time interval $\delta t$ corresponds to an atmospheric range bin $\delta R = c \cdot \delta t/2$, where $c$ is the speed of light and the factor $1/2$ is required because the light has to travel forth and back. Therefore, the chosen time interval determines the vertical resolution of the measurement. Because one height profile would have a insufficient signal to noise ratio (SNR), lidar signals are normally averaged over tens or up to thousands of profiles, depending on the research question, to get a larger number of photons per height channel and hence reduce the statistical error. The time resolution therefore results from the pulse repetition rate and the number of averaged profiles. The high temporal and vertical resolution of the measurements and the potential of covering the height range from close to the ground to more than 100 km altitude make up the attractiveness of lidar instruments. According to Weitkamp, 2006, if only using elastic scattering and neglecting the received background radiation one can write the lidar equation as follows,

$$P(r) = K\, G(r)\, \beta(r)\, T(r). \tag{1.4}$$

Where the detected power $P$ in the distance $r$ is dependent on four factors. The first factor, $K$, denotes the performance of the lidar system - the overall outgoing power - and the second, $G(r)$, is a range-dependent geometric factor. These factors are of technical origin and depend only on the used system setting and can be adjusted individually. The information of the atmosphere, and thus all the measurable quantities, are contained in the last two factors of Eq. 1.4. $\beta(r)$ is the backscatter coefficient at distance $r$ and describes the ability of the atmosphere to scatter light. $T(r)$ is the transmission term and describes how much light gets lost on the way from the lidar to distance $r$ and back. Both $\beta(r)$ and $T(r)$ are of geophysical interest and are unknown.

To be more precise, the performance of the lidar system depends on

$$K = P_O \frac{c\tau}{2} A\eta, \tag{1.5}$$

where $P_0$ is the average power of a single laser pulse, and $\tau$ is the temporal pulse length. Hence, $c\tau$ is the length of the inspected volume and $E_0 = P_0\tau$ is the pulse energy. $A$ is the area of the receiver unit - the telescope - and $\eta$ is the overall system efficiency. The factor $1/2$ appears again because the laser pulse is "folded" at the backscatterer. The geometric factor

$$G(r) = \frac{O(r)}{r^2} \tag{1.6}$$

includes the laser-beam receiver-field-of-view overlap function $O(r)$, which describes geometric factors such as the orientation of the lidar beam and telescope. The signal decreases with distance squared ( $r^{-2}$) because the receiving area is a part of a sphere's surface with radius $r$ around the scatterer. If the investigated region is far away, the photon-counting technique is often used because of the fast decaying signal.
The backscatter coefficient is generally a function of distance, wavelength and scattering angle $\beta(r, \lambda, \theta)$ as well as the type of scattering. This is the primary atmospheric parameter that determines the strength of the lidar signal and describes how much light is scattered. Since for lidarists only the backscattering in the line of sight is important, the scattering angle $\theta = 180°$. Furthermore, all following discussed parameters are strongly dependent on the wavelength, but since only a small wavelength band is of interest this fact can be neglected. Let $N_j$ be the concentration of scattering particles of kind $j$ in the volume illuminated by the laser pulse, and $d\sigma_{j,\mathrm{sca}}/d\Omega$ the particles' differential scattering cross section for the backward direction. The backscatter coefficient can then be written as

$$\beta(R) = \sum_j N_j(R) \frac{d\sigma_{j,\mathrm{sca}}}{d\Omega}, \tag{1.7}$$

with summing over all kinds of scatterers. The number concentration is given in units of $\mathrm{m}^{-3}$ and the differential scattering cross section in $\mathrm{m}^2\,\mathrm{sr}^{-2}$. Hence, the backscatter coefficient has the unit $\mathrm{m}^{-1}\,\mathrm{sr}^{-1}$. In the atmosphere, the laser light is scattered by air molecules and particulate matter, i.e., $\beta(R)$ can be written as

$$\beta(r) = \beta_{\mathrm{mol}}(r) + \beta_{\mathrm{aer}}(r). \tag{1.8}$$

Atmospheric nitrogen and oxygen molecules are mainly responsible for molecular scattering (index mol). They primarily depend on air density and thus decreases with height, i.e., backscattering decreases with distance if the observation is made from the ground. Particulate scattering (index aer for aerosol particles) is highly variable in the atmosphere on all spatial and temporal scales. Possible spreaders are for example large hydrometeors such as ice crystals forming NLCs.
A practical way to determine $\beta_{\mathrm{aer}}$ is to use the backscatter ratio (BSR), which is defined

as the ratio of total backscattered signal to signal caused by molecular scattering.

$$\mathrm{BSR} = \frac{\text{total signal}}{\text{molecule scattering}} = \frac{\beta_{\mathrm{aer}} + \beta_{\mathrm{mol}}}{\beta_{\mathrm{mol}}} \tag{1.9}$$

Rewriting Equation 1.9 and utilizing that the molecular backscatter coefficient $\beta_{\mathrm{mol}} = \sigma\rho$ with $\sigma$ being the scattering cross section of air and $\rho$ being the number density, gives a direct equation to determine $\beta_{\mathrm{aer}}$. In the following a event with a high backscatter coefficient is sometimes referred to as a strong event.

$$\beta_{\mathrm{aer}} = (\mathrm{BSR} - 1) \cdot \beta_{\mathrm{mol}} = (\mathrm{BSR} - 1)\sigma\rho \tag{1.10}$$

Lastly, the transmission term $T(r)$ considers all transmission losses of the light. $T(r)$ can take values between 0 and 1 and is given by

$$T(r, \lambda) = \exp\left(-2 \int_0^r \alpha(r, \lambda) dr\right). \tag{1.11}$$

This term results from the specific form of the Lambert–Beer–Bouguer law for lidar. $\alpha(r, \lambda)$ is the extinction coefficient and combines all transmission losses. It is defined in a similar way as the backscatter coefficient as the product of number concentration and extinction cross section $\sigma_{j,\mathrm{ext}}$ for each type of scatterer $j$. The factor 2 and integration to distance $r$ indicates the forth and back of the light beam. For a detailed derivation and representation of the equations, please see Weitkamp, 2006.

Equation 1.8 indicates that both, the molecular- and the aerosol backscatter coefficient, are equally weighted. This raises the question why the received signal from the NLC is still strong enough for the analysis even though significantly more molecular scatterers than aerosol scatterers are present. However, the scattering efficiency ($c_{\mathrm{sca}} / \pi a^2$) is dependent on the particle size and the investigated wavelength. Since the wavelength $\lambda$ is constant for our purpose, the sizeparameter $x = 2\pi a / \lambda$ is only a function of the characteristic radius $a$. For small scatterers ($x < 0.5$) the light frequency is well below the resonance frequency of the scattering particle (normal dispersion regime), and the amount of scattering is inversely proportional to the fourth power of the wavelength. This process is called Rayleigh scattering. Scattering by particles similar to, or larger than, the scattered wavelength is typically treated by the Mie theory. The boundary case to very large sizeparameters is the geometrical optics, where the value of the stray efficiency strives towards two without any size and wavelength dependencies. Figure 1.2 summarizes these phenomena. For this reason the relatively few NLC scatterers produce a larger and better measurable lidar signal than the molecular scatterers in the occurring NLC height.

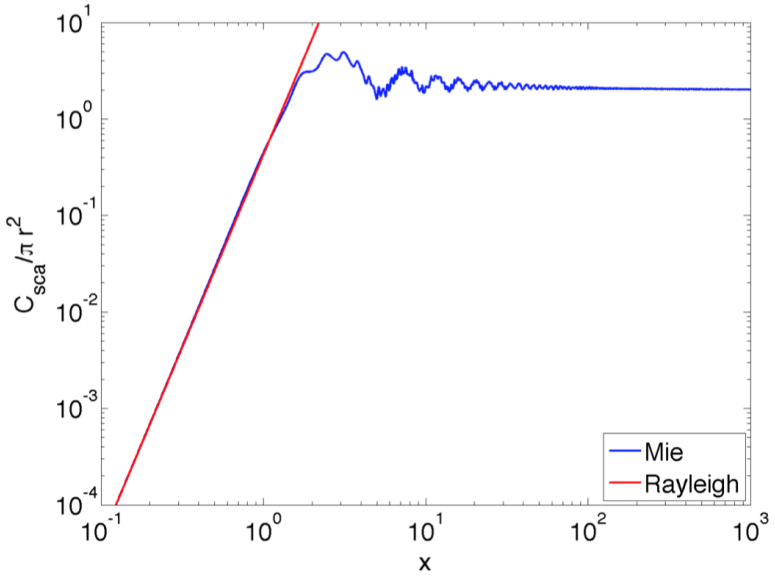


Figure 1.2: Dependency of the scattering efficiency (scattering cross section per projected surface area of the particle) on the scale parameter $x$. Figure courtesy of Manfred Brath (University of Hamburg).

# 2 Data and Methods

## 2.1 Data Selection

For a first overview, every NLC observed with the daylight capable RMR lidar at Kühlungsborn is plotted with a resolution of 33 s in time and 195 m in height, but smoothed over typically $\pm 7$ min and $\pm 1$ height bin. The cases to be investigated were manually selected from these plots from all NLC events measured with the new lidar system according to the following criteria. The selected events need to have a high backscatter coefficient which allows the higher resolution, the length of the strong NLC period should be 1 hour or more and ideally without measurement gaps due to clouds. Finally, there should be strong vertical displacements of the NLC layers, as it indicates GW presence. In the end, three cases were selected. First, two events from 2019 (June 21, 20:28 UTC to 22:58 UTC and in the night from June 23, 23:25 UTC to June 24 at 00:40 UTC) which are the strongest events ever measured in Kühlungsborn (evaluated on the basis mentioned above) were selected. In addition, they vary strongly in height over time and show clearly defined and strongly diffuse layers. Also, a third case from 2013 was selected. It occurred on June 10 from 19:40 UTC to 20:40 UTC and was the strongest NLC event that year.

## 2.2 Lidar in Kühlungsborn

In Kühlungsborn, a new, daylight-capable IAP Rayleigh–Mie–Raman lidar was developed in 2009/2010 (Gerding et al., 2016). The transmitter mainly consists of a flashlamp-pumped, injection-seeded Nd:YAG (neodymium-doped yttrium aluminum garnet) laser with a wavelength of 1064 nm and its second at 532 nm are used. The seeder is locked onto a iodine absorption line to ensure a high frequency stability. Due to the lower signal-to-noise ratio (SNR) of the main harmonic only the second harmonic at 532 nm is used for this investigation. Active beam stabilization based on correction of the outgoing beam, performed by a tilting Piezo-coupled mirror, is used to minimise the effects of turbulence on the laser beam propagation and the alignment of the telescope field of view and laser. To measure during daytime and investigate the higher atmosphere, this lidar systems utilize a chopper, which opens the field of view only when light from the region of interest arrives. This and an electronic gating are blocking the strong backscatter signal from the lower atmosphere to avoid an overload of the detectors. Also, the field of view of the telescope is as small as 62 $\mu$rad, to capture as few sun photons as possible. In addition, special filtering methods are used to suppress the solar background radiation.

Furthermore, a low beam divergence of 50 $\mu$rad is used. Lastly, multiple filtering techniques reduce the full width at half maximum to about 4 pm. A further description of the system is given in Gerding et al., 2016.

## 2.3 Processing and Methods

The further analysis is based on the backscatter coefficient, but since the data is given in photon counts, due to the high measurement distance (as described in Section 1.4) the data must be converted. Thus, this section will give an overview over all steps and assumptions that are necessary to proceed.

### 2.3.1 Preprocessing

Every 33 seconds (averaged over 1000 laser pulses with a pulse repetition frequency of 33 Hz), photon counts per height bin (15 m resolution), ranging from the ground up to 240 km, are given. In the following, these are referred to as raw data. Exemplary, a profile of the raw data up to 100 km is shown in Figure 2.1a. The signal below 37.5 km is trimmed away by the chopper and the electronic gating. Above an exponential drop with height is visible, which is due to the decreasing density and the $r^{-2}$ dependency. An elevated signal can be seen at an altitude of about 80 km. This is the noctilucent cloud. Above is an almost concise signal, which is called background, where photons are measured occasionally. Since the background radiation contributes to the signal at all heights, an average of the signal above 120 km is subtracted from the entire profile. To compensate the quadratic decrease of the signal with the height, a correction is made for each profile. The correction for the $r^{-2}$ dependency, see green line in Figure 2.1b, is normalized to a height of 50 km for a more convenient value range. Further on, the backscatter coefficient is calculated using the backscatter ratio BSR as described in Section 1.4. The used density profile (Picone et al., 2002) is fitted at a height of 65 km. This is exemplary shown as the red line in Figure 2.1b. A profile of the backscatter coefficient is shown in Figure 2.1c, where for better illustration only the height segment with the NLC is shown. This preprocessing is done for each profile and collectively they result in a Hovmöller diagram, which shows the height evolution of the NLC over time. One can be seen for June 21, 2019 in Figure 2.2 and both other events in the Appendix (Chapter 5) in Fig. 5.1.

### 2.3.2 Multi layer Analysis

The aim of this analysis is to get an quantitative overview of how many layers in the NLC are occurring, what is the distance between them and how they vary with time. For this analysis, only the event from June 21, 2019 is used, because one can manually recognize very pronounced layers, which is not the case for the others. The absence of layers can

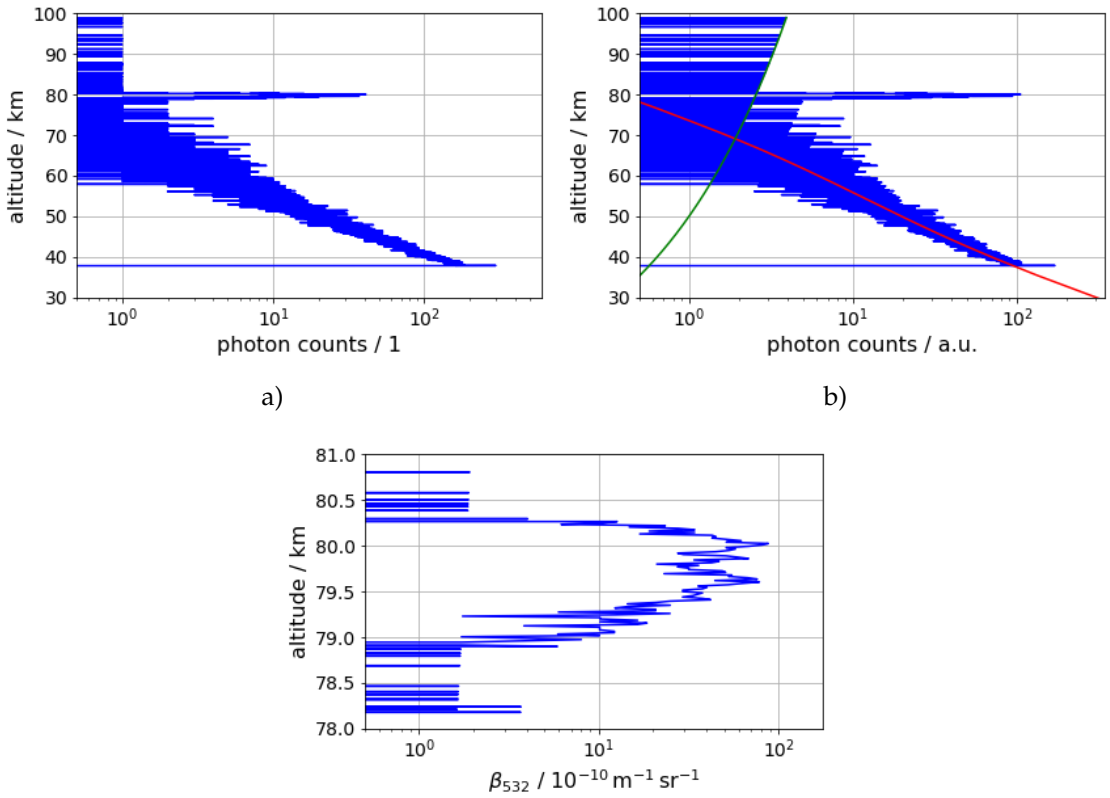


Figure 2.1: Profile of a) the raw photon counts, b) the range corrected profile without background (blue) with the envelope for the range correction (green) and the fitted MSIS profile (red) and c) the backscatter coefficient at 532 nm are shown for June 21, 2019 at 22:10 UTC. Notice that the height range in c) is different for a better display of the NLC.

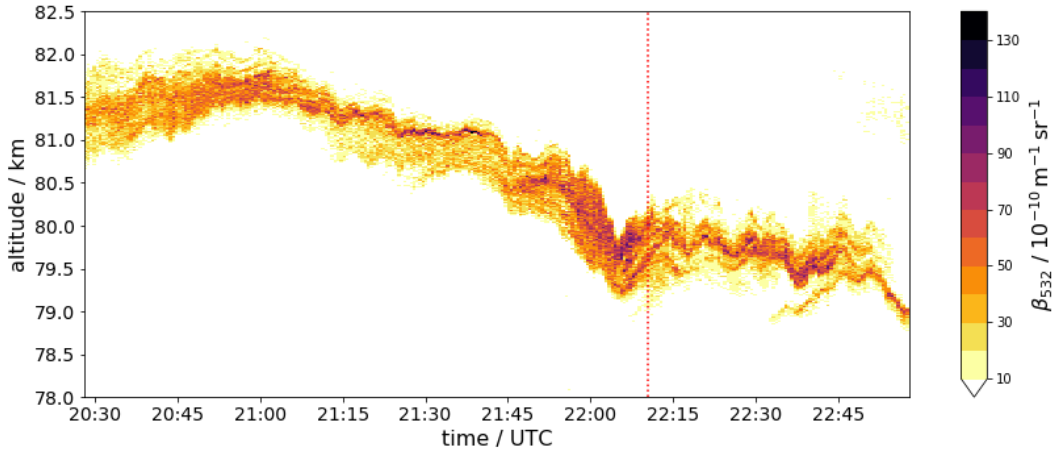


Figure 2.2: Backscatter coefficient for the NLC event from June 21, 2019, 20:28 - 22:58 UTC. The data has a resolution of 33 s and a vertical bin width of 15 m. The red dashed line indicates the time for which the profiles in Fig. 2.1 are displayed. The color scale represents the NLC backscatter coefficient at 532 nm $\beta_{532}$.

be due to the weaker backscatter coefficient and therefore the reduced ability to dissolve finer structures or simply because no layers were present.
Using the clouds as a tracer for neutral air motions is limited to timescales where the particle size does not change too much, because the backscatter coefficient depends on the sixth power of the particle size. Since size changes of these particles depends on the dynamic features and the transport of energy and momentum by GW, the assumption is made that the cloud layers and induced structures are changing in the order of the Brunt-Väisälä period of about 5 minutes (under the given conditions). In order to reduce numerical errors, the data was smoothed with a running average, which has a width of the Brunt-Väisälä period. Faster variations are not of interest, since the influence of gravity waves is to be investigated and these have (at least intrinsically) longer periods. Afterwards, for each smoothed profile, the number of significant maxima were counted using the scipy module integrated in Python (The function used is called "scipy.signal.find_peaks" and following parameter were used: prominence $= 10$, width $= 5$). In addition, the vertical extension of the cloud is defined as the distance between the highest and lowest height bin, where the backscatter coefficient is at least an eighth of the profile maximum. Thus a mean distance between the layers can be determined from the vertical extension of the cloud and the number of layers.

### 2.3.3 Spectral Analysis

To determine a temporal spectrum of vertical movements, the maximum of the backscatter coefficient was used as robust tracer for vertical motion. For a multi-layer event, the condition that the cloud must not move more than 15 bins per profile has been introduced to prevent a back and forth jumping between two layers. Poly-fits up to the fourth order were done (using the Python numpy package) and the best fitting one for the base height reduction. As a measure the root mean square error ($RMSE = \sqrt{\frac{1}{N}\sum_{i=1}^{N}(y_i - \hat{y}_i)^2}$) was used. For the spectral analysis itself, the Discrete Fourier Transform with the Chuck-Norris-Fast FFT algorithm, which is embedded in the Python numpy package was used. The Nyquist-frequency is the theoretical maximum of a physically meaningful interpreted frequency and is half of the maximum sampling frequency. However, since gravity waves must have a intrinsic frequency between $|f|$ and $N$ ($\sim 0.003\,\mathrm{s}^{-1}$ and $0.00012\,\mathrm{s}^{-1}$, respectively) these are the frequency boundaries of interest.

# 3 Results and Discussion

## 3.1 Statistical Analysis

The NLC event of June 21, 2019 appears to have the finest resolved structures. This is partly due to the fact that it is the longest of those three events and therefore one time bin in the plots is displayed smaller relative to the others. The main reason, however, is that this is the strongest event ever measured in Kühlungsborn and the conditions were optimal (the event begins 38 minutes after sunset, hence there is close to no solar radiation). This results in a high mean signal-to-noise ratio of about 103. Due to the low noise level, for example, between 21:20 and 21:40 a thin, strongly defined layer becomes clearly distinguishable from an actually very diffuse layer. In addition, a signal with a high SNR is more feasible to analyse with algorithms, since individual outliers do not interfere with the analysis. For this reason, most of the investigation in this thesis will be based on this particular event. The other two events have an SNR of 35 (June 10, 2013) and 64 (June 23, 2019), respectively. Figure 3.1a shows the combined height distribution of all three events. The most frequent altitude corresponds exactly to the climatological average altitude of 82.75 km above Kühlungsborn (Luebken et al., 2008) (note that for the evaluation the centroid altitude and not the height of the peak backscatter coefficient was used). The event of June 21, 2019, however, has an average height of 80.6 km. Thus, this event occurred on a of 2 km lower altitude compared to the climatology.

The vertical extension or the thickness of the NLC of all events combined is below average as seen in Figure 3.1b. This, however, is biased due to the selection criteria that the clouds must have strong vertical displacements. Those displacements are more visible in a shallow, more defined layer than in a diffuse cloud. Hence mean cloud thickness is below average. The average vertical extent is 0.6 km $\pm$0.1 km for the individual events. On June 23, 2019 the vertical extent was most variable with time. Both a shallow, strong defined layer (at around 23:35 UTC) and one vast, diffuse layer occurred (after midnight). These different types of NLC can be found in images taken by NLC cameras. For example, at an NLC event near Trondheim on August 1, 2009, a very well-defined layer with recognizable wave structures appeared, which can be seen in the upper half of Figure 3.2. In contrast, in the lower half of the image a diffuse layer with very few wave patterns can be seen.

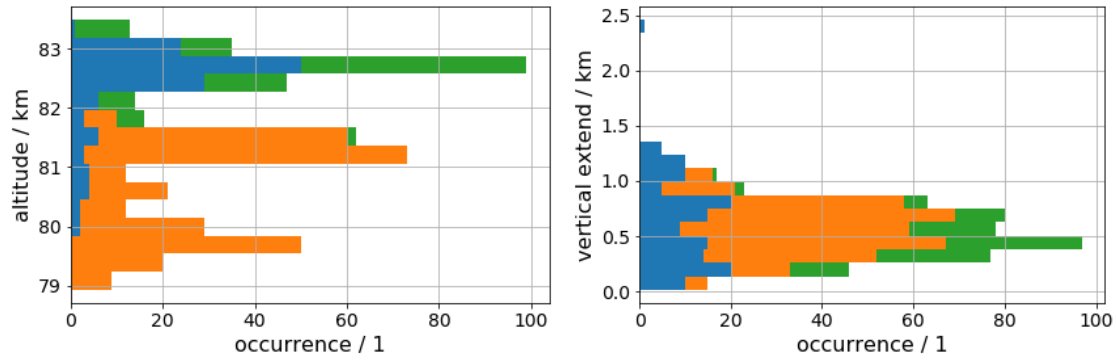


a) b)

Figure 3.1: Number of occurrences of a) maximum backscatter coefficient per height range and b) the vertical extension of the NLC for all three events is shown. The colors green, orange and blue indicate the events of June 10, 2013, June 21, 2019 and June 23, 2019, respectively.


Figure 3.2: NLC event from August 01, 2009 23:07 UTC captured by the IAP NLC Camera in Trondheim.

Figure 3.3 shows the distribution of the layer thicknesses of the strongest layer. This is not representative either, because, as described above, events with a rather smaller thickness and a defined layer were selected. The average layer thickness of all three cases considered is 225 m and 44.1 % of the time the layer thickness is less than the previously used vertical resolution of 195 m. Since many structures appear on smaller vertical scales, it is advisable to choose a higher resolution, if the the strength of an event allows it.

## 3.2 Multi layer Analysis

This section deals with the event from 21 June, 2019, where several clear layers with vertical distances of less than 1 km were clearly visible. That has never before been observed in Kühlungsborn. These are clearly visible in upper figure in Fig. 3.4. For example, at about 22:15, where a local minimum of the backscatter coefficient of less than 20 (units and order of magnitude are omitted here and in the following for better readability) lies

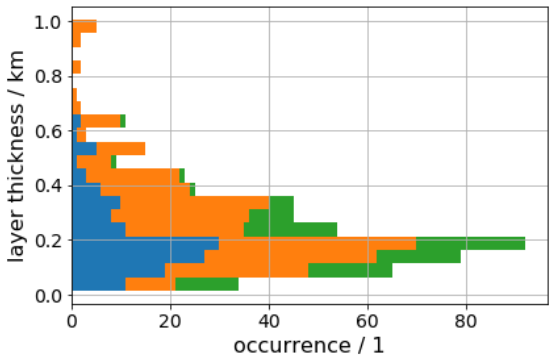


Figure 3.3: Number of occurrence of the layer thickness of the layer with the strongest backscatter coefficient for all three events is shown. The colors green, orange and blue indicate the events of June 10, 2013, June 21, 2019 and June 23, 2019, respectively.

between two layers with a beta of more than 60. Towards the end of the cutout, a second layer is nearing to the main layer from below. Although these features are not described by the algorithm in the same way as they are read manually, they are sufficient for the analysis. A time evolution of the number of layers calculated by the algorithm can be seen in the middle figure of Fig. 3.4, for reference. The lowest figure in Fig. 3.4 shows the vertical extent of the cloud, i.e. the vertical distance between the two altitudes where the backscatter coefficient has reached a threshold of $1/e$ of the maximum considered from above and below the NLC. This consideration has an obvious weakness, i.e. at 22:23, where a peak of the signal can be seen. This peak is caused by the one bin above the NLC with a beta of over 30. This could be a very weak layer above the NLC or just noise. The algorithm for the determination of the number of layers has difficulties at this point in time to decide whether two layers are present or not. If divided by the respective vertical expansion in cases where two or more layers occur, a rough estimate of an average layer distance can be obtained. This estimation indicates a mean distance of the layers of about 265 meters. A similar value is achieved by a rough manual estimation. However, gravity waves at these altitudes have vertical wavelengths in the order of 10 km (Fritts et al., 1988). A plausible explanation would be static instabilities, which one would have to examine further.

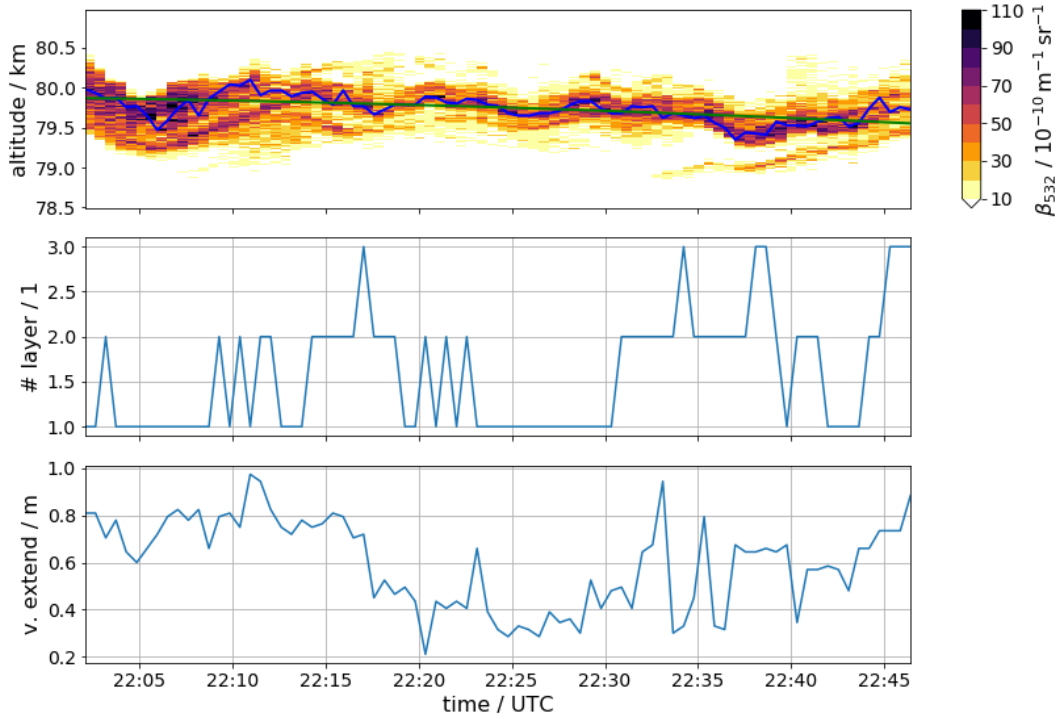


Figure 3.4: The upper Figure shows the backscatter coefficient for the NLC event from June 21, 2019, 22:03 - 22:46 UTC with a resolution of 33 s and a vertical bin width of 15 m. The blue line indicates the traced maximum of $\beta_{532}$ and the green line the polyfit used as the base of the FFT. The second and third Figure are showing the number of layers in the NLC and the vertical extend of the NLC, respectively.

## 3.3 Spectral Analysis

The NLC event of 21 June, 2019 was also selected for spectral analysis, as the manual observation of this event already showed many wave structures. These can be seen particularly well in the period from about 22:15 to 22:35 UTC. A wave period of about 6-7 minutes, which corresponds approximately to a frequency of about 0.003 Hz, can thus be determined. The power spectra of the height of the maximum backscatter coefficient, which is shown as a blue line in Figure 3.4, were calculated. In addition, the polyfit for the base of the FFT is shown as a green line in the same figure. The result of the spectral analysis is shown in Figure 3.5, where the power spectral densities of all three events are shown as a function of frequency and depicted as solid lines. It must be noted that these are not the intrinsic frequencies, since they may be Doppler shifted. One could validate how big this effect is by using wind measurements. The green dashed line represents the mean slope of -2.6 of the three gradients. As a reference, the theoretical slopes of turbulent spectra and a GW spectra are shown as red dotted lines. The theoretical slope of a turbulent spectrum is described by Kolmogorov-Obukhow theory (Zakharov et al., 2012), where a dimensional analysis shows that the energy of the wave is dependent on the wavevector $k$ to the power of ($-5/3$). According to Nastrom and Gage, 1985, the spectral slope steepens at larger scales and approaches -3. This is considered as a limit for large scale gravity waves. Thus, the spectrum indicates large scale GW, since the slope is with approximately -3 close to the Nastrom-Gage spectrum. However, the time periods are very short to make representative statements about the spectrum, since here single frequencies dominate. The previously manually determined frequency of about 0.003 Hz at the event from June 21, 2019 can be found in the figure as a peak in the power density at the referred frequency (see blue line in Fig. 3.5). More cases must be investigated for a smoother and more representative spectrum. At low frequencies, the spectrum decreases with a slope of -3. This fits very well with the theory of large scale waves. In addition, it can be recognized that the slope of the spectrum flattens towards larger frequencies and becomes turbulent (-5/3). If the spectrum could be resolved to very small time scales of less than 10 seconds, the spectrum would be completely flattened by the solar background radiation and photon counting noise.

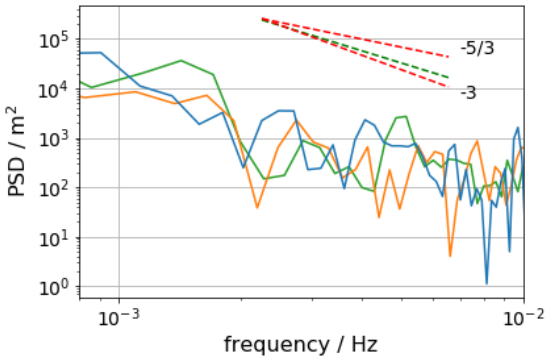


Figure 3.5: Power spectral density for the events June 10, 2013 (green solid line), June 21, 2019 (orange solid line) and June 23, 2019 (blue solid line) is shown within the frequency domain between the Coriolis frequency |f| and the Brunt-Väisälä frequency N (some larger frequencies are shown due to a possible Doppler shift). In addition the theoretical slopes for a GW (-3) and turbulent spectra (-5/3), shown as red dashed lines, and the mean slope of the three events (green dashed line) are shown for comparison.

# 4 Conclusions

## Summary

For the first time, lidar measurements with a resolution of 33 s in time and 15 m in height from Kühlungsborn were used to investigate noctilucent clouds and how gravity waves are modulating them. In this thesis, the theoretical background for noctilucent clouds, gravity waves and lidar was summarized. Then, the used data and instruments were described, as well as the used methods. In addition, the preprocessing of the data was described in detail. It was found that the strongest event ever measured in Kühlungsborn, which occurred on June 21, 2019, was located more than 2 km lower than the climatological average of 82.75 km. 44 % of the layers and structures are thinner than the previous resolution of 195 m, which might be biased by the selection of cases investigated. In addition to these thin structures, it was also found that on June 21, 2019 two or more layers are arranged on top of each other with a mean vertical distance of 265 m. This has never been observed before in Kühlungsborn. The reasons for such appearances are unknown, but it is suspected that instabilities play a major role in the formation. The spectral analysis showed that the power spectrum has an average slope of -2.6 for the investigated cases. Such a spectrum is characteristic for large scale GW, but turbulence signatures could be found. Finally, it can be said that strong NLC events can be used to investigate GW with high resolution lidar measurements in Kühlungsborn.

## Outlook

There are many alternative approaches how to use high resolution lidar data to gain more and deeper knowledge about gravity waves in mid latitudes.
First, with each further measurement a higher sample size is obtained. This would lead to a smoother and more representative spectrum and it could be verified if the slope of the power spectrum remains typical for large scale GW. In addition, one could apply the Lomb-Scargle method that makes it possible to determine a frequency spectrum despite measurement gaps (see Lomb, 1976; Scargle, 1982). A wavelet transformation could also be used to investigate how the frequency spectrum changes over time. Since winds are completely neglected in this thesis, one could determine the intrinsic frequencies and compare the therefrom calculated wave number better with existing literature. The wind estimation could be done with lidar or radar measurements.
In addition, one could use cameras to observe noctilucent clouds and could determine the

horizontal wavelength based on these images. If possible simultaneously, so one could verify whether there are large scale GW. This could also be compared with satellite data. High resolution temperature profiles would be necessary to test the hypothesis that multi layers are caused by static stability. However, this is not yet possible with today's technology on these resolutions. A completely different approach would be to reverse model these multi layers so that one can predict possible causes by the model conditions.

# Acknowledgement

First of all, I would like to thank Prof. Dr. Franz-Josef Lübken from the Leibniz-Institute of Atmospheric Physics in Kühlungsborn. He gave me the opportunity to write this bachelor thesis at the IAP in the first place. Michael Gerding is my secondary supervisor for the thesis, but he was my primary contact for any topic-related content. He was never tired of explaining the theoretical background or showing and describing the lidar system and associated principles. He always had an open ear and steered me in the right direction, but still made it possible for this thesis to be my own work.
Furthermore, I would like to thank Prof. Dr. Stefan Bühler for being my primary supervisor although the topic is rather unrelated to his field of study. I was always welcome in his office and he provided me helpful insights in the process of writing and other generic skills.
Finally, I must express my thankfulness to my parents Helke Stammerjohann and Dirk Petersen, to my family and all my friends without whose support throughout the writing process and the whole 3 years of the bachelor program it wouldn't have been so much fun, or even possible. Special thanks to Florian Römer and Philine Podein, who reviewed this thesis and gave me a new approach if I got stuck with writing. Moreover, I would like to thank Ralf Wedemann, Imke Schirmacher, Malina Klatt and everybody else who came to my office, motivated me or forced me to take a short break and get fresh back to work afterwards.

# Bibliography

Craig, Richard A (2016). *The upper atmosphere: meteorology and physics*. Elsevier.

Fritts, David C and M Joan Alexander (2003). "Gravity wave dynamics and effects in the middle atmosphere". In: *Reviews of geophysics* 41.1.

Fritts, David C, Steven A Smith, Ben B Balsley, and C Russell Philbrick (1988). "Evidence of gravity wave saturation and local turbulence production in the summer mesosphere and lower thermosphere during the STATE experiment". In: *Journal of Geophysical Research: Atmospheres* 93.D6, pp. 7015–7025.

Geller, Marvin A, M Joan Alexander, Peter T Love, Julio Bacmeister, Manfred Ern, Albert Hertzog, Elisa Manzini, Peter Preusse, Kaoru Sato, Adam A Scaife, et al. (2013). "A comparison between gravity wave momentum fluxes in observations and climate models". In: *Journal of Climate* 26.17, pp. 6383–6405.

Gerding, M, M Kopp, P Hoffmann, J Höffner, and F-J Lübken (2013). "Diurnal variations of midlatitude NLC parameters observed by daylight-capable lidar and their relation to ambient parameters". In: *Geophysical Research Letters* 40.24, pp. 6390–6394.

Gerding, Michael, J Höffner, J Lautenbach, M Rauthe, and F-J Lübken (2008). "Seasonal variation of nocturnal temperatures between 1 and 105 km altitude at 54° N observed by lidar". In: *Atmospheric Chemistry and Physics* 8.24, pp. 7465–7482.

Gerding, Michael, Maren Kopp, Josef Höffner, Kathrin Baumgarten, and Franz-Josef Lübken (2016). "Mesospheric temperature soundings with the new, daylight-capable IAP RMR lidar". In: *Atmospheric Measurement Techniques* 9.8, pp. 3707–3715.

Holton, James R (1973). "An introduction to dynamic meteorology". In: *American Journal of Physics* 41.5, pp. 752–754.

Holton, James R and M Joan Alexander (2000). "The role of waves in the transport circulation of the middle atmosphere". In: *Atmospheric science across the stratopause* 123, pp. 21–35.

Jesse, Otto (1896). "Die höhe der leuchtenden nachtwolken". In: *Astronomische Nachrichten* 140, p. 161.

Kim, Young-Joon, Stephen D Eckermann, and Hye-Yeong Chun (2003). "An overview of the past, present and future of gravity-wave drag parametrization for numerical climate and weather prediction models". In: *Atmosphere-Ocean* 41.1, pp. 65–98.

Li, Tao, C-Y She, Han-Li Liu, Thierry Leblanc, and I Stuart McDermid (2007). "Sodium lidar–observed strong inertia-gravity wave activities in the mesopause region over Fort Collins, Colorado (41° N, 105° W)". In: *Journal of Geophysical Research: Atmospheres* 112.D22.

Lomb, Nicholas R (1976). "Least-squares frequency analysis of unequally spaced data". In: *Astrophysics and space science* 39.2, pp. 447–462.

Ludlam, Frank Henry (1957). "Noctilucent clouds". In: *Tellus* 9.3, pp. 341–364.

Luebken, Franz-Josef, Gerd Baumgarten, Jens Fiedler, Josef Hoeffner, and Uwe Berger (2008). "Does the mean NLC altitude vary with latitude?" In: *37th COSPAR Scientific Assembly*. Vol. 37, p. 1837.

Nastrom, GD and K So Gage (1985). "A climatology of atmospheric wavenumber spectra of wind and temperature observed by commercial aircraft". In: *Journal of the atmospheric sciences* 42.9, pp. 950–960.

Picone, JM, AE Hedin, D Pj Drob, and AC Aikin (2002). "NRLMSISE-00 empirical model of the atmosphere: Statistical comparisons and scientific issues". In: *Journal of Geophysical Research: Space Physics* 107.A12, SIA–15.

Riggin, Dennis, David C Fritts, Clinton D Fawcett, and Erhan Kudeki (1995). "Observations of inertia-gravity wave motions in the stratosphere over Jicamarca, Peru". In: *Geophysical research letters* 22.23, pp. 3239–3242.

Scargle, Jeffrey D (1982). "Studies in astronomical time series analysis. II-Statistical aspects of spectral analysis of unevenly spaced data". In: *The Astrophysical Journal* 263, pp. 835–853.

Shepherd, Theodore G (2000). "The middle atmosphere". In: *Journal of Atmospheric and Solar-Terrestrial Physics* 62.17-18, pp. 1587–1601.

Størmer, Carl (1935). "Measurements of Luminous Night Clouds in Norway 1933 and 1934. With 3 Figures in the Text and 17 Plates". In: *Astrophysica Norvegica* 1, p. 87.

Vestine, Ernest Harry (1934). "Noctilucent Clouds (with Plate VI)". In: *Journal of the Royal Astronomical Society of Canada* 28, p. 249.

Weitkamp, Claus (2006). *Lidar: range-resolved optical remote sensing of the atmosphere*. Vol. 102. Springer Science & Business.

Zakharov, Vladimir E, Victor S L'vov, and Gregory Falkovich (2012). *Kolmogorov spectra of turbulence I: Wave turbulence*. Springer Science & Business Media.

# 5 Appendix

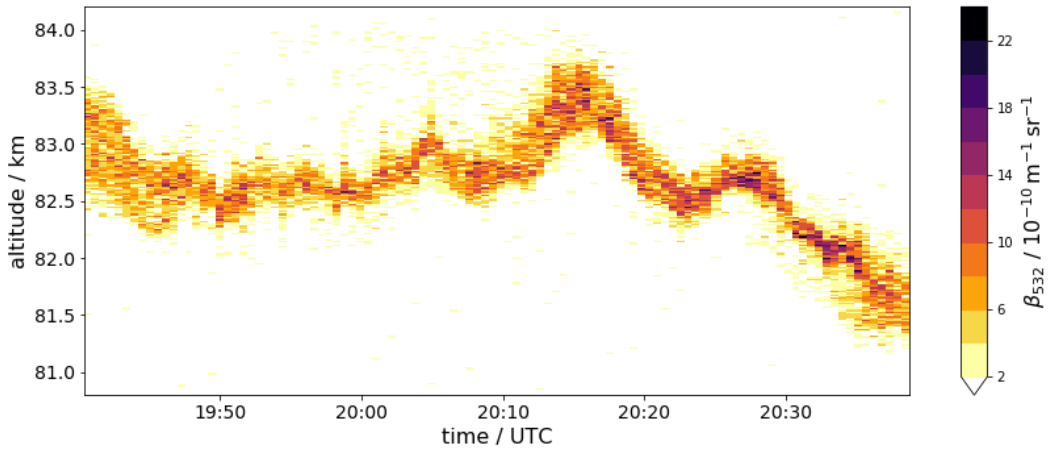


a)

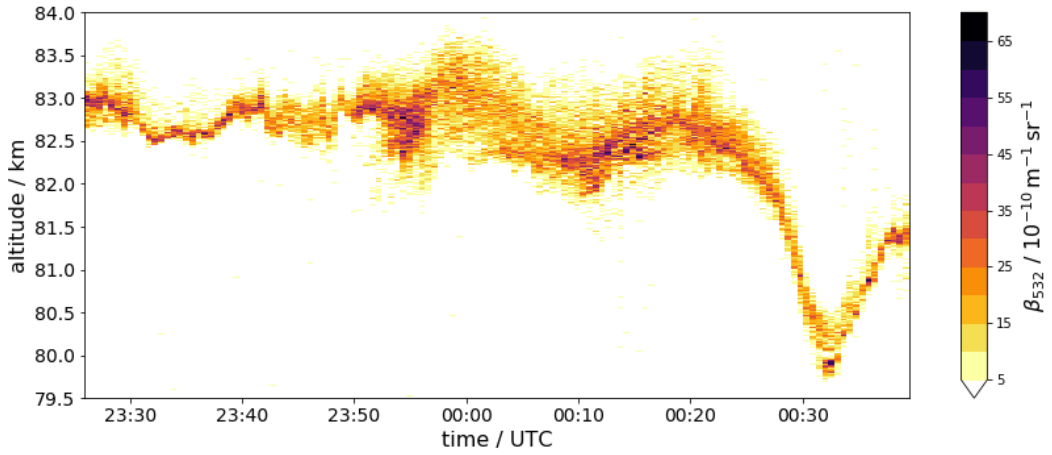


b)

Figure 5.1: Backscatter coefficient for NLC event from a) June 10, 2013, 19:40 - 20:40 UTC and b) the night from June 23, 23:25 UTC to June 24, 00:40 UTC in 2019. The data has a resolution of 33 s and a vertical bin width of 15 m. The color scale represents the NLC backscatter coefficient at 532 nm $\beta_{532}$ in $10^{-10}/(\mathrm{m} \cdot \mathrm{sr})$. Notes the different color scale limits.

# Eidesstattliche Versicherung

Hiermit versichere ich an Eides statt, dass ich die vorliegende Arbeit im Studiengang B.Sc. Meteorologie selbstständig verfasst und keine anderen als die angegebenen Hilfsmittel – insbesondere keine im Quellenverzeichnis nicht benannten Internet-Quellen – benutzt habe. Alle Stellen, die wörtlich oder sinngemäß aus Veröffentlichungen entnommen wurden, sind als solche kenntlich gemacht. Ich versichere weiterhin, dass ich die Arbeit vorher nicht in einem anderen Prüfungsverfahren eingereicht habe und die eingereichte schriftliche Fassung der auf dem elektronischen Speichermedium entspricht.
Ich bin mit einer Einstellung in den Bestand der Bibliothek des Fachbereiches einverstanden.

Hamburg, den _____ Unterschrift: _____